(Received 28 April 2026, Accepted 25 June 2026, Scheduled 30 July 2026)

Torque Ripple Suppression for a Novel Asymmetric External Rotor Permanent Ferrite-Assisted Synchronous Reluctance Motor

Chaozhi Huang, Wen Kuang*, Fangrong Wang, Ji Zhang, and Zhihong Liu

School of Electrical Engineering and Automation, Jiangxi University of Science and Technology, Ganzhou, Jiangxi 341000, China

ABSTRACT: To address the problems of flux barriers' excessive torque ripple and complicated multi-parameter optimization in conventional permanent magnet-assisted synchronous reluctance motors (PMa-SynRMs), this study proposes a novel asymmetric external-rotor ferrite-assisted synchronous reluctance motor (AERFa-SynRM). By adopting an asymmetric magnet shifting arrangement, the magnetic circuit configuration is optimized, which improves air-gap flux density and permanent magnet torque without increasing material and manufacturing costs. The magnetic circuit characteristics and torque generation mechanism of symmetric and asymmetric rotor structures are compared and analyzed by establishing mathematical and electromagnetic models. Taking key rotor geometric parameters as design variables and average torque, torque ripple, and efficiency as multi-objective optimization indices, a BP-Kriging hybrid surrogate model is constructed, and the NSGA-II algorithm is adopted for global parameter optimization. The finite element simulation results demonstrate that the proposed asymmetric rotor structure can effectively enhance air-gap flux density and no-load back-EMF performance. After multi-objective optimization, the average torque and motor efficiency are greatly improved, while the torque ripple is sharply reduced. The asymmetric angle adjustment realizes the peak-valley mutual cancellation between permanent magnet torque and reluctance torque, which fundamentally suppresses electromagnetic torque ripple. The proposed topology and collaborative optimization strategy provide an effective solution for improving the performance and reducing the torque ripple of low-cost ferrite PMa-SynRMs.

1. INTRODUCTION

In recent years, the prices of rare-earth permanent magnet materials have continued to rise, driven by stricter resource controls, rising demand for high-end products, and supply chain volatility [1, 2]. Conventional permanent magnet synchronous motors (PMSMs) rely on neodymium-iron-boron (NdFeB) magnets for excitation, leading to high material costs and heavy rare-earth dependence. In contrast, a permanent magnet-assisted synchronous reluctance motor (PMa-SynRM) integrates a small number of permanent magnets into a rotor multi-layer flux-barrier structure for auxiliary excitation. This configuration substantially reduces manufacturing costs and rare-earth usage while achieving a high saliency ratio, wide speed regulation range, high efficiency, and excellent torque performance. Accordingly, PMa-SynRMs have been widely applied in electric vehicles, industrial automation, household appliance drives, and other high-performance fields [3–6].

Nevertheless, PMa-SynRM exhibits a low power factor and high torque ripple. Its multi-layer flux-barrier topology also complicates design optimization, making it difficult to obtain optimal parameters [7, 8]. Researchers have investigated structural modifications and parametric optimization to reduce torque ripple. An asymmetric modular stator-rotor arrangement was proposed to suppress the 12th- and 2nd-order torque harmonics. Torque ripple can be reduced through stator partitioning, flux-gap regulation, asymmetric flux barriers, and end-slot shifting [9]. Axial rotor segmentation was adopted to cancel the torque harmonics between the permanent magnet torque and reluctance torque, with further performance improvement through neural-network-based optimization [10]. A new asymmetric hybrid-pole rotor was developed to narrow the phase difference between peaks of the permanent magnet and reluctance components using pole-shifting effects, simultaneously boosting torque and suppressing ripple [11]. An asymmetric concentrated-flux rotor was designed to use the flux-concentrating effects and peak-trough misalignment of torque components, lowering ripple while maintaining high torque density and stable operation [12].

Algorithm-driven optimization of key motor parameters can effectively suppress torque ripples while improving average torque and operating efficiency. The differential evolution (DE) algorithm was used to refine the rotor slot and flux-barrier layouts of the external rotor PMa-SynRM, mitigating torque ripple and cogging torque, and improving torque characteristics [13]. A multi-objective optimization framework based on Kriging was established for electric motors. When integrated with a preset driving cycle, it optimizes motor design, reduces operational losses, and improves the overall drive-system efficiency [14]. A hybrid optimization scheme combining a back-propagation (BP) neural network surrogate model and multi-objective genetic algorithm (MOGA) was applied to an in-wheel external-rotor permanent magnet motor, lowering the

* Corresponding author: Wen Kuang (6120240696@mail.jxust.edu.cn).

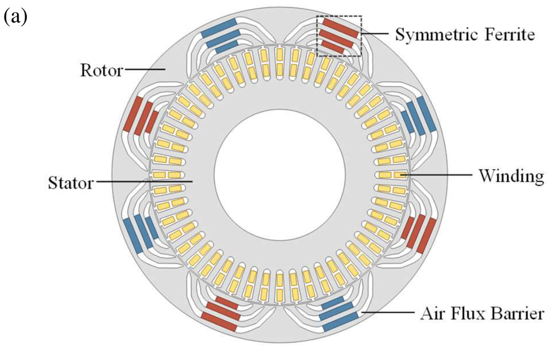

FIGURE 1. Topology diagram. (a) Symmetric rotor and (b) asymmetric rotor.

armature thermal load and core losses and enhancing the operational performance [15]. Multi-objective optimization coupled with multi-physics analysis was implemented for the automotive axial-flux PMa-SynRM, simultaneously improving the electromagnetic performance and thermal management [16]. The response surface methodology and multi-objective particle swarm optimization were combined to optimize a bearingless permanent magnet synchronous motor, enhancing both the torque and suspension performance [17].

However, existing studies still have clear limitations. On the one hand, most asymmetric rotor and magnet-shifting schemes are targeted at interior-rotor rare-earth permanent magnet motors, while research on low-speed external-rotor ferrite-assisted PMa-SynRMs is relatively scarce; the torque ripple suppression mechanism based on the length-difference offset of multilayer permanent magnets remains to be further explored. On the other hand, traditional single surrogate models, such as Kriging, suffer from reduced prediction accuracy under high-dimensional design variables, which cannot satisfy the high-precision modeling requirements of complex multi-layer flux barrier structures. Overall, there is still a lack of systematic research that integrates asymmetric rotor topology design and high-precision hybrid surrogate model optimization for low-speed external-rotor ferrite PMa-SynRMs, which constitutes the core research gap this work aims to fill.

To fill the above research gap, this study proposes a novel asymmetric external rotor ferrite-assisted synchronous reluctance motor (AERFa-SynRM). A parametric analysis model is developed, and the magnetic circuit and electromagnetic performance of the proposed motor are compared with those of the conventional symmetric rotor topology. Key rotor structural parameters are selected as design variables, aiming to maximize average torque, minimize torque ripple, and maximize operating efficiency. A high-precision BP-Kriging surrogate model is constructed by integrating a BP-based autoencoder to enhance the conventional Kriging approach. The Non-dominated Sorting Genetic Algorithm II (NSGA-II) is adopted to perform global optimization on the established model and determine the optimal design. Finally, finite element simulation is carried out to compare air-gap flux density, no-load back-EMF, electromagnetic torque, and other key indices before and after optimization. Results verify the superior overall electromagnetic performance of the optimized motor.

2. MOTOR STRUCTURE AND OPERATING PRINCIPLE

2.1. Motor Structure

This study presents a novel asymmetric external rotor ferrite-assisted synchronous reluctance motor (AERFa-SynRM). Fig. 1 shows the symmetric and asymmetric rotor topologies. In an asymmetric rotor, permanent magnets are asymmetrically shifted to adjust the magnetic path. Because the magnet material and total volume remain nearly unchanged, the asymmetric rotor design does not increase the material or manufacturing costs.

A hybrid method combining straight lines and curve functions was adopted to construct rotor flux barriers [18]. Rectangular side flux barriers were used in this design to simplify magnet insertion. As depicted in Fig. 2, D_1 denotes the distance from the center of the central rectangular flux barrier to the rotor center; L_1 and W_1 are the length and width of the central flux barrier; L_{s1} and W_{s1} are the length and width of the side flux barriers; R_1 is the distance from the end of the side flux barrier to the rotor center; and a_1 is the opening angle of the flux barrier.

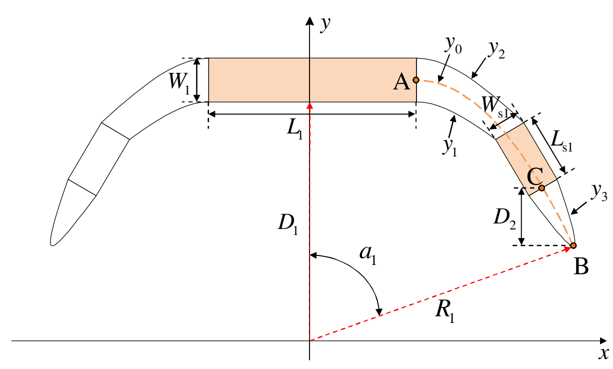

FIGURE 2. Improved flux-barrier structure.

Curves y_1, y_2, and y_3 are parabolic. Each parabola is determined by its vertex and one additional point on the curve. Parabola y_0 is built with Point A as the vertex and Point B as the second point on the parabola. Point A is the right midpoint of the central flux barrier. Point B is the lower end of the side flux barrier. This parabola defines the spatial position of the side flux barrier.

$$y_0 = k\left(x - \frac{L_1}{2}\right)^2 + D_1 + \frac{W_1}{2} \tag{1}$$

$$k = \frac{R_1 \cos\alpha_1 - D_1 - \dfrac{W_1}{2}}{\left(R_1 \sin\alpha_1 - \dfrac{L_1}{2}\right)^2} \tag{2}$$

Point C is the midpoint of the lower rectangular edge and is located on the parabola. D_2 defines the vertical distance between Point C and Point B. The slope of the rectangular side equals the tangent slope of the parabola at Point C. With the given length and width of the flux barrier, the four vertex coordinates of the rectangle can be determined. Parabolas y_1, y_2, and y_3 are then generated from these coordinates to model one full layer of flux barriers. The same modeling procedure was applied to the other two layers.

Each rotor pole contains three flux barrier layers. Ferrite permanent magnets were embedded inside each barrier layer. Table 1 lists the design parameters of the proposed prototype.

TABLE 1. Main design parameters of AERFa-SynRM.

Parameter Name	Unit	Value
Outer radius of stator	mm	170
Outer radius of rotor	mm	220
Stack length	mm	35
Air gap length	mm	0.8
Rated speed	r/min	350
Rated voltage	V	48
Number of turns	–	14
Pole / slot	–	8/48

The stator and rotor cores are transversely stamped from DW310_50 silicon steel, which has a material density of $7600\,\mathrm{kg/m^3}$ and a stacking factor of 0.95. The hysteresis loss coefficient $k_h = 155$ and eddy current loss coefficient $k_e = 0.822$ are used for core loss calculation in finite element simulation. The adopted permanent magnet is Y40 ferrite with remanence of 0.39 T and coercivity of 175 kA/m at room temperature, and the armature winding material is copper with conductivity of 5.96×10^7 S/m at 20°C.

2.2. Operating Principle

Reluctance torque arises from the inductance difference between the rotor's d- and q-axes. Permanent magnets inside the rotor create a magnetic field. This field couples with the armature field from stator windings to generate permanent-magnet torque. The total electromagnetic torque is the sum of reluctance torque and permanent-magnet torque, as expressed in the following formula:

$$T_e = \frac{3}{2}p(\psi_{PM} i_q + (L_d - L_q) i_d i_q) \tag{3}$$

Flux linkage and voltage mathematical models of the AERFa-SynRM can be expressed as follows:

$$u_d = \frac{d\psi_d}{dt} - \omega\psi_q + Ri_d \tag{4}$$

$$u_q = \frac{d\psi_q}{dt} + \omega\psi_d + Ri_q \tag{5}$$

The flux linkage formulas are:

$$\psi_d = L_d i_d + \psi_{PM} \tag{6}$$

$$\psi_q = L_q i_q \tag{7}$$

where u_d and u_q are the d-axis and q-axis components of the stator voltage; ψ_d and ψ_q are the d-axis and q-axis components of the stator flux linkage; i_d and i_q are the d-axis and q-axis components of the stator current; L_d and L_q are the d-axis and q-axis inductances; ψ_{PM} is the flux linkage generated by the permanent magnet; ω is the electrical angular velocity of the motor; T_e is the electromagnetic torque; p is the number of pole pairs.

The symmetric structure mainly optimizes the distribution of rotor permanent magnets with only small adjustments to flux barrier sizes. Fig. 3 presents the magnetic circuit model and equivalent magnetic circuit under no-load conditions.

Neglecting magnetic flux leakage, the main magnetic fluxes of symmetric and asymmetric structures are expressed as:

$$\Phi_{sym} = \frac{F_{sym}}{R_{sym}} \tag{8}$$

$$\Phi_{asym} = \frac{F_{asym}}{R_{asym}} \tag{9}$$

In these formulas, F_{sym} and F_{asym} are the total magnetomotive forces of permanent magnets in the two structures. These values are nearly equal when the total magnet volume remains unchanged. R_{sym} and R_{asym} are the equivalent magnetic reluctance of symmetric and asymmetric magnetic circuits, which can be calculated as:

$$R_{sym} = 2\sum_{i=1}^{3} R_{pmi} + R_{gd} + R_{drp} \tag{10}$$

$$\begin{aligned} R_{asym} &= R_{pms3} + R_{pms2} \parallel (R_{pm2} + R_{pm1}) \\ &\quad + \sum_{i=1}^{3} R_{pmi} + R_{gd} + R_{drp} \end{aligned} \tag{11}$$

By rearranging the permanent magnets, portions of the magnetic circuit change from series to parallel. The magnetic reluctance of permanent magnets can be expressed by Formula (12):

$$R_{pm} = \frac{W_{pm}}{\mu_0 \mu_r l_{ef} L_{pm}} \tag{12}$$

$$\psi_{asym} = N\Phi_{asym} \tag{13}$$

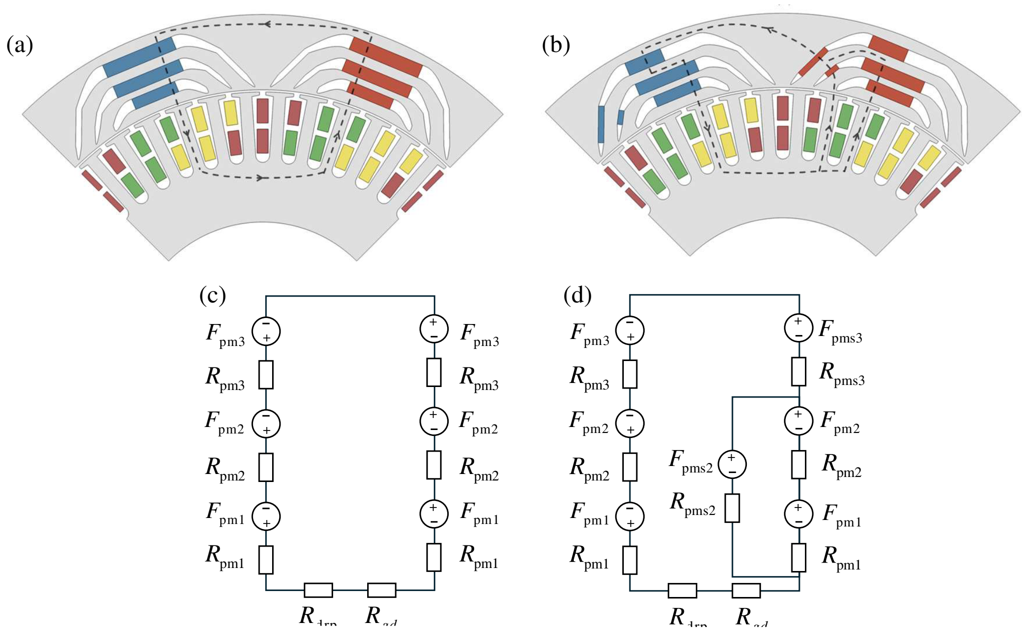

FIGURE 3. Magnetic circuit models and simplified equivalent models. (a) Magnetic circuit model of symmetrical motor, (b) asymmetric motor magnetic circuit model, (c) equivalent magnetic circuit of symmetrical motor, and (d) equivalent magnetic circuit of asymmetric motor.

In this formula, l_{ef} is the motor stack length; L_{pm} is the length of permanent magnets; W_{pm} is the width of permanent magnets. From Formulas (8) to (13), proper adjustment of L_{pm} and W_{pm} can greatly reduce R_{asym} compared with R_{sym}. This results in a significantly higher main flux Φ_{asym} than Φ_{sym}.

Based on Formula (3), electromagnetic torque is the sum of permanent magnet torque and reluctance torque. The asymmetric rotor increases the main air-gap flux Φ_{asym}. This increase raises permanent magnet flux linkage ψ_{pm} and enhances output electromagnetic torque. The motor's torque performance is thus enhanced.

3. MOTOR OPTIMIZATION DESIGN

3.1. Optimization Objective and Design Variables

Average torque, torque ripple, and efficiency are core performance metrics for evaluating AERFa-SynRMs. These metrics directly determine the motor's output capability, operational stability, and cost-effectiveness. They must be comprehensively considered during design optimization. Higher average torque provides stronger load capacity. Excessive torque ripple can cause vibration and noise and reduce system reliability. Efficiency reflects energy utilization efficiency. Low efficiency increases energy consumption and operating costs, limiting its use in energy-saving applications. This study takes the above three metrics as optimization objectives: the average torque and operating efficiency are set as maximization objectives, and the torque ripple is set as a minimization objective. The multi-objective optimization problem and corresponding design constraints are formally expressed in Formula (14):

$$\begin{cases} \max & T_{\text{avg}} \\ \min & T_{\text{rip}}\,\% \\ \max & \eta\,\% \end{cases} \quad \text{s.t.} \quad \begin{cases} T_{\text{avg}} \geq 7\text{ Nm} \\ T_{\text{rip}} \leq 10\,\% \\ \eta \geq 70\,\% \end{cases} \tag{14}$$

Torque ripple (T_{rip}) is defined as the ratio of the output torque's peak-to-peak value to the average torque (T_{avg}) within a single electrical cycle. The formula is:

$$T_{\text{rip}} = \frac{T_{\max} - T_{\min}}{T_{\text{avg}}} \times 100\% \tag{15}$$

The efficiency calculation model is based on the principle of energy conservation and the method of separating losses; the efficiency formula can be expressed as:

$$\eta = \frac{P_{out}}{P_{in}} \times 100\% = \frac{P_{out}}{P_{out} + P_{loss}} \times 100\% \tag{16}$$

$$P_{loss} = P_{cu} + P_{fe} + P_{fw} \tag{17}$$

The total losses of the motor include copper losses (P_{cu}), iron losses (P_{fe}), and miscellaneous losses (P_{fw}). Quantitative calculation of each loss component is performed using electromagnetic-field finite-element simulation and loss-separation formulas. The detailed calculation rules are as follows: the stator copper loss includes only the Joule loss caused by winding resistance; the iron loss is computed using the Bertotti model with the hysteresis and eddy current loss coefficients of DW310_50 silicon steel; and the miscellaneous loss, treated as stray loss, is simplified to 1%–2% of the total output power based on empirical engineering formulas.

The rotor flux barrier structure of the AERFa-SynRM is complex, with various parameter combinations. The shape and size of flux barriers significantly affect electromagnetic performance. This study selects ten parameters strongly correlated with motor performance as design variables. With the targets of low torque ripple, high average torque, and high efficiency, optimization algorithms are used to generate different rotor geometries. Finite element analysis software is used to com-

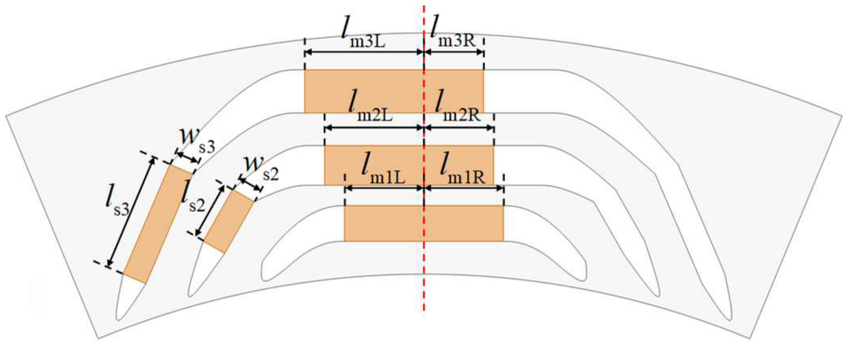

FIGURE 4. Rotor geometric parameter model of AERFa-SynRM.

pare electromagnetic performance before and after optimization. The optimal motor design that satisfies design requirements is finally determined. The design variables are shown in Fig. 4.

Reasonable ranges are set for the ten highly relevant design variables. Specific value ranges are listed in Table 2.

The design variables l_{m1L}/l_{m1R}, l_{m2L}/l_{m2R}, and l_{m3L}/l_{m3R} denote the left and right extension lengths of the permanent magnets (PMs) in the 1st to 3rd flux barriers, respectively, measured relative to the pole centerline. In the initial symmetric prototype, the PMs are arranged symmetrically about the pole centerline with equal left and right lengths in each layer, and this configuration serves as the performance baseline for comparison throughout the study. In the present study, the overall asymmetric shift of the PMs is achieved by deliberately adjusting the left-right length difference, and the total torque ripple is mitigated via the complementary cancellation between the peaks and valleys of the PM torque and reluctance torque waveforms. As verified by preliminary parametric sweeps, shifting the third-layer PMs exerts the most significant regulatory effect on torque ripple, with the optimal suppression performance attained when l_{m3R} lies within the range of -2 mm to 2 mm, provided that magnetic circuit rationality and manufacturing feasibility are preserved. The multi-objective optimization conducts a global search over prescribed asymmetric parameter intervals; baseline symmetric values are adopted solely for performance benchmarking and are intentionally excluded from the optimization search space. Consequently, no logical conflict arises between the parameter settings of the symmetric and asymmetric configurations.

3.2. BP-Kriging Surrogate Model of the Motor

The Kriging model is a linear, unbiased, minimum-variance interpolation surrogate model. It is widely used in motor optimization. The core strengths include high-precision fitting with small sample sizes and the ability to estimate prediction variance. It decomposes the output response into a global trend term and a local random deviation term [19]. The mathematical expression is as follows:

$$y(x) = f(x)^{\mathrm{T}}\beta + z(x) \tag{18}$$

In the formula, $x \in R^n$ is an n-dimensional vector of input design variables; $f(x)$ is a polynomial basis function; β is a vector of regression coefficients; and $z(x)$ is a stationary Gaussian random process whose covariance structure satisfies:

$$\begin{cases} E[z(x)] = 0 \\ \mathrm{Cov}[z(x_i), z(x_j)] = \sigma^2 R(\theta, x_i, x_j) \end{cases} \tag{19}$$

In the formula, $R(\theta, x_i, x_j)$ is the spatial correlation function; in this study, a cubic polynomial correlation function is used, as shown in Formula (20):

$$R(\theta_k, x_{ik}, x_{jk}) = \begin{cases} 1 - 3\xi_k^2 + 2\xi_k^3, & \xi_k < 1 \\ 0, & \xi_k \geq 1 \end{cases} \tag{20}$$

In the formula, $\xi_k = \theta_k |x_{ik} - x_{jk}|$ represents the standardized distance. The optimal θ is estimated by maximum likelihood estimation, yielding optimal estimates of β and σ^2, as shown in Formulas (20)–(22). The prediction formula for the unknown point is given in Formula (23):

$$\beta = (F^{\mathrm{T}} R^{\mathrm{T}} F)^{-1} F^{\mathrm{T}} R^{\mathrm{T}} Y \tag{21}$$

$$\hat{\sigma}^2 = \frac{1}{m}(Y - F\beta)^{\mathrm{T}} R^{-1} (Y - F\beta) \tag{22}$$

$$\hat{y}(x^*) = f(x^*)^{\mathrm{T}}\beta + r^{\mathrm{T}}(x^*) R^{-1}(Y - F\beta) \tag{23}$$

The conventional Kriging model is prone to the curse of dimensionality when facing high-dimensional variables. It leads to lower prediction accuracy and fails to meet the demands of multi-variable modeling for motors. To solve this problem, a BP-based autoencoder is introduced for nonlinear feature extraction. It can remove variable redundancy and coupling and provide low-dimensional, highly representative input features for the Kriging model.

The BP-based autoencoder is an unsupervised neural network with a symmetric structure. It is built on error back propagation and consists of an encoder and a decoder. The training objective is to reconstruct the input as accurately as possible, so as to extract key features with the strongest representation capacity. This study adopts a single-hidden-layer feedforward network to build the BP-based autoencoder. The network structure includes an input layer, a single hidden layer, and an output layer. The number of neurons in the input and output layers is equal to the dimension n of the original design variables. The

TABLE 2. Design variables and variation ranges.

Design variable	Description	Range
l_{m1L} (mm)	Left length of central PM, 1st-layer flux barrier	6, 9
l_{m1R} (mm)	Right length of central PM, 1st-layer flux barrier	6, 9
l_{m2L} (mm)	Left length of central PM, 2nd-layer flux barrier	9, 12
l_{m2R} (mm)	Right length of central PM, 2nd-layer flux barrier	9, 12
l_{s2} (mm)	Length of side PM, 2nd-layer flux barrier	3, 6
w_{s2} (mm)	Width of side PM, 2nd-layer flux barrier	1, 3
l_{m3L} (mm)	Left length of central PM, 3rd-layer flux barrier	9, 14
l_{m3R} (mm)	Right length of central PM, 3rd-layer flux barrier	−2, 2
l_{s3} (mm)	Length of side PM, 3rd-layer flux barrier	9, 14
w_{s3} (mm)	Width of side PM, 3rd-layer flux barrier	1, 3

number of neurons in the hidden layer can be adaptively adjusted according to data complexity.

The forward propagation process of the BP-based autoencoder is divided into two stages: encoding and decoding.

In the encoding stage, the normalized original design variable x is fed into the network. The nonlinear mapping of the encoder is used to obtain the hidden layer feature vector h, to achieve feature compression and extraction of the input data:

$$h = f_1(W_1 x + b_1) \tag{24}$$

In the formula, W_1 is the weight matrix from the input layer to the hidden layer; b_1 is the bias vector of the hidden layer; f_1 is the activation function of the hidden layer.

In the decoding stage, the hidden-layer feature vector h is fed into the decoder, and the output vector $\hat{x}$ is reconstructed through a nonlinear mapping. The calculation formula is:

$$\hat{x} = f_2(W_2 h + b_2) \tag{25}$$

In the formula, W_2 is the weight matrix from the hidden layer to the output layer; b_2 is the bias vector of the output layer; f_2 is the activation function of the output layer.

The mean squared error (MSE) between the input and output is taken as the loss function to train the network. The weights and biases of the network are updated iteratively by the back-propagation algorithm. The loss function is expressed as follows:

$$L_{\text{MSE}} = \frac{1}{m} \sum_{i=1}^{m} \|x_i - \hat{x}_i\|_2^2 \tag{26}$$

where m is the number of training samples; x_i is the i-th input sample; $\hat{x}_i$ is the network-reconstructed output of the i-th sample.

The decoder is discarded after training. Only the encoder's nonlinear mapping relationship is preserved. The original high-dimensional design variables are mapped to core features that are denoised and highly representative. These features are then used as input to the subsequent Kriging model.

All sample data are derived from finite element analysis (FEA) computational experiments. The Latin Hypercube Sampling (LHS) method is adopted to generate 250 parameter combinations within the ranges of the ten design variables specified in Table 2, ensuring uniform coverage of the design domain and reliable generalization of the subsequent surrogate model. For each parameter configuration, a 2D electromagnetic FEA model is established to compute the three optimization objectives: average torque, torque ripple, and efficiency. The FEA results serve as ground-truth references for model training and accuracy validation.

From the 250 sampled data points, 200 are randomly partitioned into the training set for the BP-Kriging model, while the remaining 50 form the independent test set. The mean absolute error (MAE) and coefficient of determination (R^2) are employed as quantitative metrics to assess the prediction accuracy and generalization capability of the surrogate model. Figs. 5–7 present the comparison between the FEA-calculated reference values and the corresponding predicted values of BP-Kriging for average torque, torque ripple, and efficiency. The resulting MAE and R^2 values for each optimization objective are tabulated in Table 3.

TABLE 3. Comparison of prediction models for each optimization objective.

Optimization objectives	Kriging		BP-Kriging	
	MAE (%)	R^2	MAE (%)	R^2
T_{avg}	1.02	0.979	0.17	0.999
T_{rip}	0.40	0.898	0.35	0.919
η	2.50	0.978	0.41	0.999

As shown in Table 3, the BP-Kriging model has a higher coefficient of determination R^2 and a lower mean absolute error (MAE) than the traditional Kriging model for the three metrics: average torque, torque ripple, and efficiency. It demonstrates superior predictive accuracy and generalization performance. Therefore, this study selects the BP-Kriging model as the surrogate model for optimization.

3.3. Multi-Objective Optimization

Three primary optimization objectives exist in motor design: maximizing average torque, minimizing torque ripple, and maximizing operating efficiency. They exhibit strong nonlinear coupling and mutual constraints. Single-objective opti-

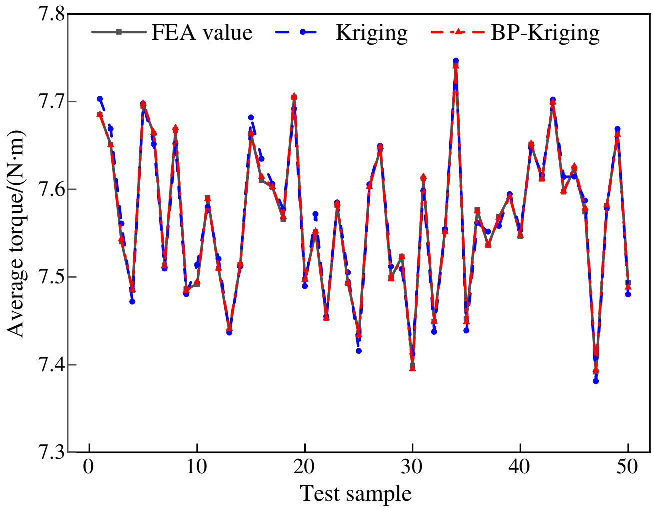

FIGURE 5. Comparison between actual and predicted values of the average torque.

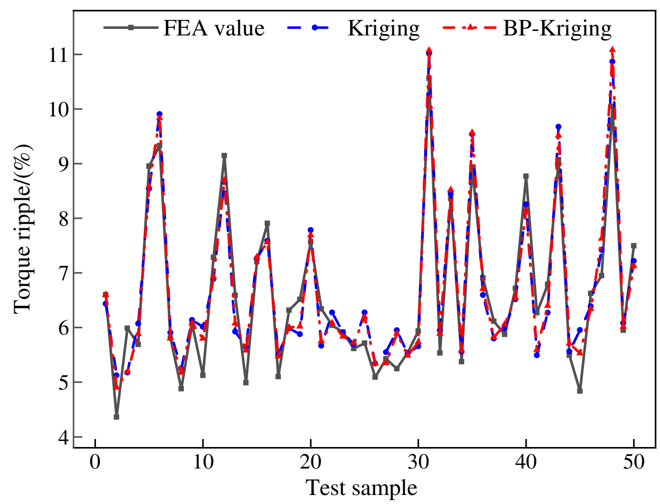

FIGURE 6. Comparison between real and predicted values of the torque ripple.

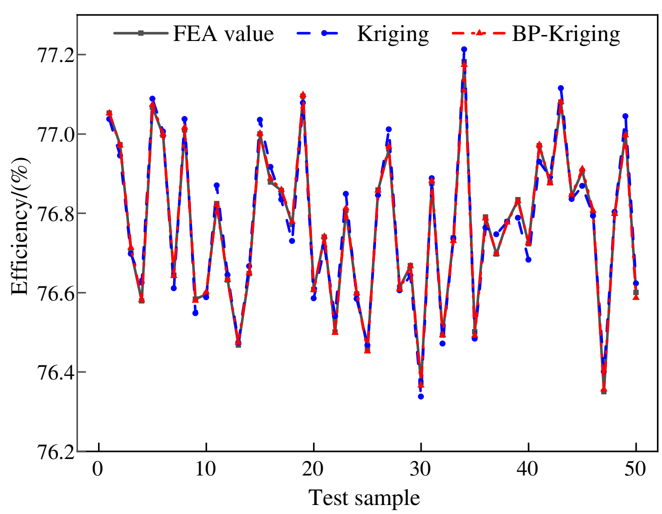

FIGURE 7. Comparison between real and predicted values of the efficiency.

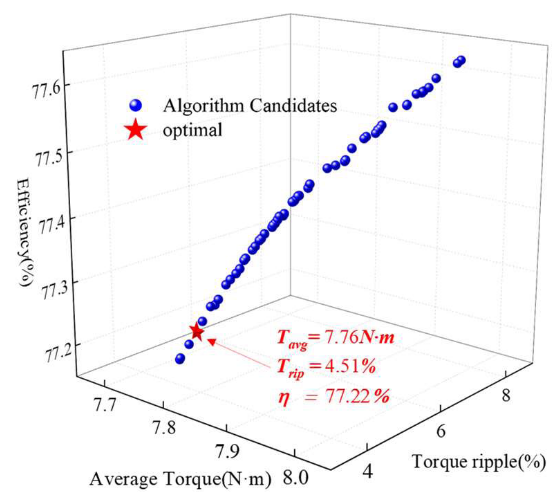

FIGURE 8. Pareto optimal front.

mization methods cannot achieve global coordinated optimization of multiple performance indices. Thus, multi-objective optimization algorithms are needed to find a Pareto-optimal solution set that balances all performance criteria.

Non-dominated Sorting Genetic Algorithm II (NSGA-II) is a classic multi-objective evolutionary algorithm based on the Pareto dominance criterion. It takes fast non-dominated sorting, crowding-distance calculation, and elite retention as core mechanisms. It effectively overcomes defects of traditional multi-objective evolutionary algorithms, including high computational complexity, weak convergence, and insufficient diversity of optimal solutions. It becomes one of the most widely used multi-objective optimization algorithms in motors' electromagnetic design optimization. The multi-objective particle swarm optimization algorithm tends to fall into a local optimum. The multi-objective differential evolution algorithm is likely to converge prematurely. NSGA-II shows better performance in global search ability, population diversity maintenance, and convergence speed [20]. Combined with the high-precision surrogate model BP-Kriging built above, the NSGA-II algorithm is used to conduct global optimization for the AERFa-SynRM's multi-objective problem. The three-dimensional Pareto optimal front is obtained as shown in Fig. 8.

All solutions on the Pareto optimal frontier are non-dominated optimal solutions. Their selection requires a comprehensive evaluation based on the motor's actual design requirements and constraints. In this work, while ensuring that average torque and operating efficiency meet the design constraints, torque ripple suppression is set as the core optimization objective. Therefore, the Pareto non-dominated solution with the best torque-ripple performance, as shown in Fig. 8, is selected as the final optimal design.

The design variables of the optimal solution are input into finite element software for simulation. The predicted values of the surrogate model are compared with the finite element method's simulation results, as shown in Table 4. This comparison verifies the prediction accuracy of the built BP-Kriging surrogate model and the engineering reliability of optimization

TABLE 4. Comparison of predicted and simulated values.

Parameter	Predicted value	Actual value	Error (%)
T_{avg} (N·m)	7.7604	7.7628	0.0308
T_{rip} (%)	4.5272	4.0862	10.55
η (%)	77.2282	77.2279	0.0004

results. The relative prediction errors are 0.0308% for average torque and 0.0004% for operating efficiency. This verifies the model's high predictive accuracy for core performance metrics. For torque ripple, the relative error is 10.55%, but the absolute deviation is only 0.4322 percentage points. This relatively high relative error mainly stems from the small magnitude of torque ripple. The small absolute deviation is amplified in the relative error calculation. This does not indicate a failure of the model's predictive capability. Overall, these results verify the high fitting accuracy and generalization ability of the BP-Kriging surrogate model. They also confirm that the optimization results based on the NSGA-II algorithm have good accuracy and engineering applicability.

Table 5 compares values of design variables and core performance indices of the motor before and after optimization. It proves the effectiveness of the proposed optimization method in improving the core performance of the AERFa-SynRM. It also shows that the method can be effectively applied to electromagnetic design and the AERFa-SynRM's optimization process.

4. COMPARISON OF MOTOR PERFORMANCE

4.1. No-Load Characteristics Analysis

The finite element method is used for comparative simulations between the AERFa-SynRM's symmetric and asymmetric rotor structures. The analysis mainly focuses on magnetic field distribution, no-load back-EMF, and torque characteristics. The permanent magnet volume of the symmetric rotor is $8476.6\,\text{mm}^3$. The permanent magnet volume of the asymmetric rotor is $8402.1\,\text{mm}^3$. The total volume of permanent magnets is reduced by $74.5\,\text{mm}^3$.

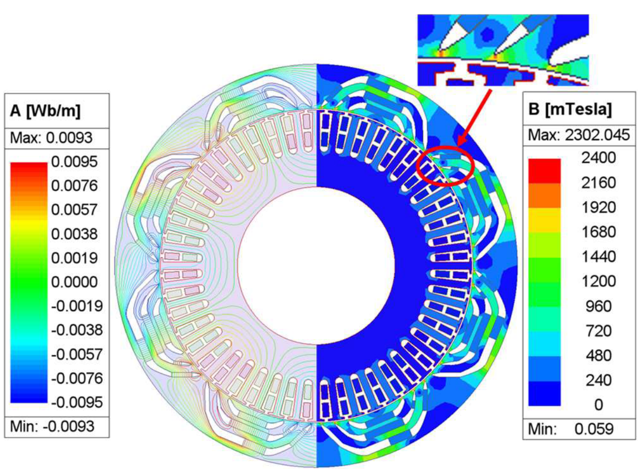

FIGURE 9. Magnetic flux density contour plot and magnetic field line distribution diagram of the motor.

Figure 9 shows the AERFa-SynRM's no-load flux density distribution. Core saturation and magnetic field lines in the motor core are evenly distributed. The flux density reaches its maximum at the rotor ribs, approximately 2.3 T. Fig. 10 shows the no-load air-gap flux density waveforms of the two models. The motor with an asymmetric rotor structure exhibits a much higher air-gap flux density than that with a symmetric rotor structure. The fundamental air-gap flux density is increased by 21.89% compared with the symmetric rotor, as shown in Figure 11. Meanwhile, the asymmetric structure exhibits lower harmonic components at the 7th, 9th, 13th, and 15th orders. Other harmonic orders are relatively higher.

Figures 12 and 13 illustrate the no-load back-EMF and harmonic analysis results of the two AERFa-SynRM models. The fundamental back-EMF of the asymmetric motor rises from 5.6 V to 6.9 V, an increase of 23.21% compared to the symmetric motor. The torque output capability is improved accordingly.

4.2. Load Characteristics Analysis

Figure 14 presents the simulated relationship between torque and rotor position before and after optimization under rated working conditions. The initial motor provides an average torque of 7.29 N·m and a torque ripple of 12.28%. The optimized motor provides an average torque of 7.76 N·m and a torque ripple of 4.09%. The average torque is increased by 6.05%. The torque ripple is reduced by 66.69%.

To quantitatively elucidate the torque composition and the underlying ripple-suppression mechanism of the proposed asymmetric rotor design, the total electromagnetic torque and its decomposed components of both the baseline symmetric and the proposed asymmetric structures are compared in Fig. 15. In the figure, Total(Sym) and Total(Asym) represent the total electromagnetic torque of the symmetric reference and the proposed asymmetric structures, respectively; Reluctance(Sym) and Reluctance(Asym) denote the decomposed reluctance torque components, while PM(Sym) and PM(Asym) correspond to the permanent magnet (PM) torque components. The subscript "Sym" refers to the original symmetric baseline structure, and "Asym" refers to the proposed asymmetric rotor with circumferentially offset permanent magnets.

The torque component decomposition is implemented via the frozen-permeability method. As a well-validated standard approach for saturated electrical machines, this method accurately incorporates magnetic saturation and cross-coupling effects [21]. For the proposed Y40 ferrite-assisted synchronous reluctance motor, the global core saturation level is moderate, with high-flux regions localized only at the rotor ribs, which guarantees the method's satisfactory accuracy for mechanism-level analysis. For the baseline symmetric topology, the PM torque features negligible ripple; accordingly, the total electromagnetic torque ripple is predominantly governed by the reluctance torque ripple. In the proposed asymmetric design, the reluctance torque remains nearly invariant as the modification is achieved primarily through circumferential shifting of the permanent magnets, and the flux barrier geometry is largely preserved. The introduced phase mismatch between the two torque

TABLE 5. Comparison of initial and optimal design variables and performance.

	Design variables	unit	Initial value	Optimal value
Motor Specifications	l_{m1L}	mm	8	8.20
	l_{m1R}	mm	8	8.18
	l_{m2L}	mm	10	11.52
	l_{m2R}	mm	10	10.90
	l_{s2}	mm	5	4.35
	w_{s2}	mm	2	1.84
	l_{m3L}	mm	12	12.90
	l_{m3R}	mm	12	-0.25
	l_{s3}	mm	12	11.40
	w_{s3}	mm	2	2.49
Motor Performance	T_{avg}	N · m	7.29	7.76
	T_{rip}	%	12.28	4.09
	η	%	76.04	77.23

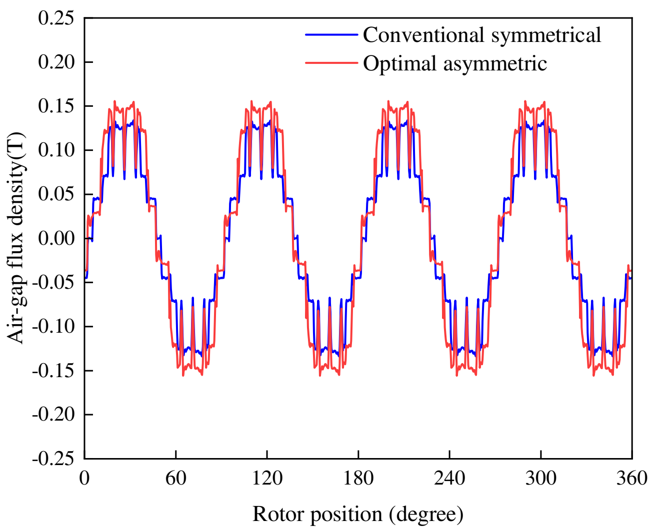

FIGURE 10. No-load air-gap flux density.

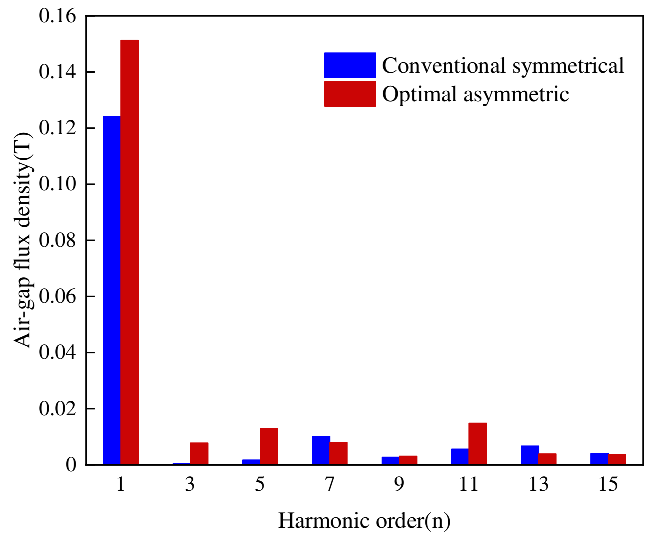

FIGURE 11. Fourier analysis of no-load air-gap flux density.

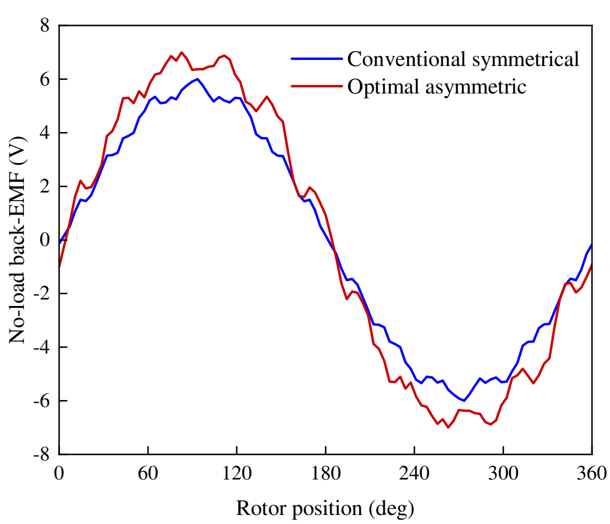

FIGURE 12. No-load back-EMF.

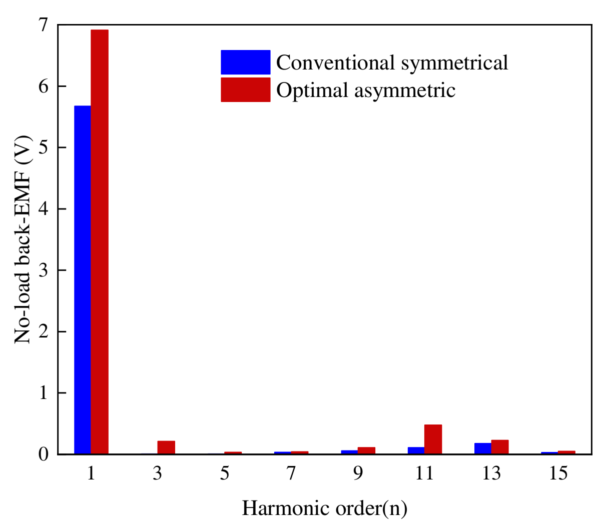

FIGURE 13. Fourier analysis of no-load back-EMF.

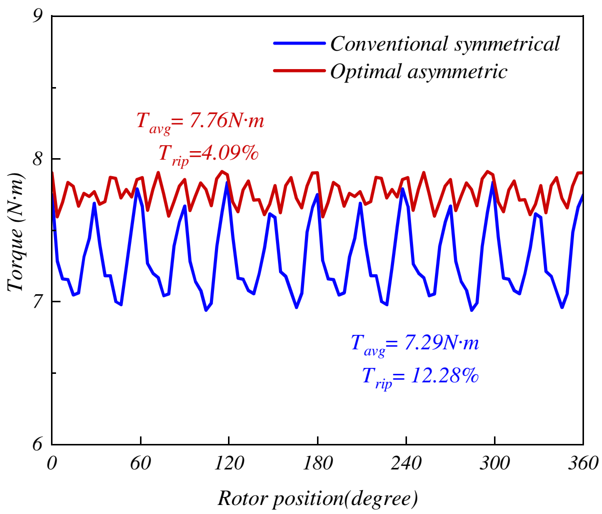

FIGURE 14. Electromagnetic torque waveform.

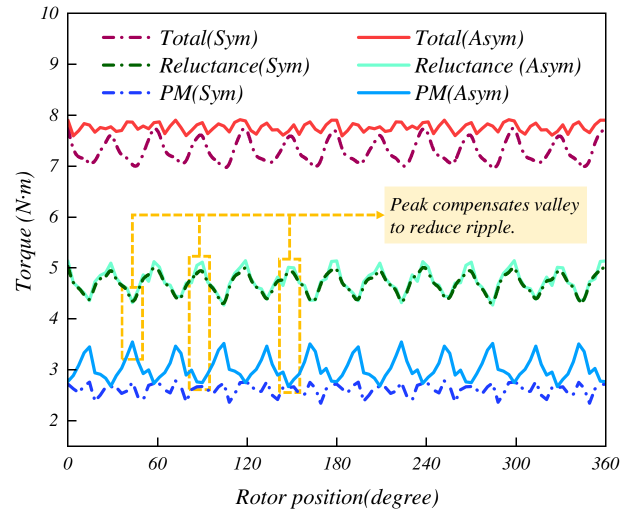

FIGURE 15. Reluctance torque and permanent-magnet torque.

components enables peak-valley cancellation of torque ripples, thereby effectively suppressing the total torque ripple.

5. CONCLUSION

This study investigates an asymmetric external-rotor ferrite-assisted synchronous reluctance motor. An asymmetric rotor topology and an improved flux barrier structure are presented. A high-precision BP-Kriging surrogate model is built. The NSGA-II algorithm is applied to the motor's multi-objective optimization. The finite element simulation software is used to conduct comprehensive comparisons and verifications of electromagnetic performance before and after optimization. Results show that the motor's average torque rises from 7.29 N·m to 7.76 N·m after optimization. Operating efficiency is improved from 76.04% to 77.23%. Torque ripple is suppressed significantly. It drops from 12.28% to 4.09%, a reduction of 66.69%. The proposed asymmetric rotor structure effectively improves air-gap flux density and no-load fundamental back-EMF of the motor. It allows the harmonic components of the permanent magnet torque and the reluctance torque to cancel each other. This study confirms the prediction accuracy of the BP-Kriging surrogate model and the effectiveness of the NSGA-II multi-objective optimization algorithm. The reliability of the asymmetric rotor optimal topology is also validated. The motor's comprehensive electromagnetic performance is enhanced. The work can provide a useful reference for low-ripple optimization design of other similar low-speed external-rotor motors.

REFERENCES

[1] Podmiljšak, B., B. Saje, P. Jenuš, T. Tomše, S. Kobe, K. Žužek, and S. Šturm, "The future of permanent-magnet-based electric motors: How will rare earths affect electrification?" *Materials*, Vol. 17, No. 4, 848, 2024.

[2] Brody, R. M., P. R. Ohodnicki, M. K. Ghosh, C. Macias, A. Sherman, A. Talaat, J. Cui, and B. Grainger, "Trade study for rare-earth-free interior permanent magnet synchronous machine using MnBi permanent magnets," *IEEE Transactions on Industry Applications*, Vol. 60, No. 4, 6010–6022, 2024.

[3] Bonthu, S. S. R., A. Arafat, and S. Choi, "Comparisons of rare-earth and rare-earth-free external rotor permanent magnet assisted synchronous reluctance motors," *IEEE Transactions on Industrial Electronics*, Vol. 64, No. 12, 9729–9738, 2017.

[4] Nobahari, A., A. Vahedi, and R. Nasiri-Zarandi, "A modified permanent magnet-assisted synchronous reluctance motor design for torque characteristics improvement," *IEEE Transactions on Energy Conversion*, Vol. 37, No. 2, 989–998, 2022.

[5] Pošković, E., L. Ferraris, and N. Bianchi, "Different approaches in the use of ferrites in assisted reluctance machines," *IEEE Transactions on Industry Applications*, Vol. 58, No. 5, 6136–6144, 2022.

[6] Degano, M., M. Murataliyev, W. Shuo, D. Barater, G. Buticchi, W. Jara, N. Bianchi, M. Galea, and C. Gerada, "Optimised design of permanent magnet assisted synchronous reluctance machines for household appliances," *IEEE Transactions on Energy Conversion*, Vol. 36, No. 4, 3084–3095, 2021.

[7] Xing, F., W. Zhao, and B.-I. Kwon, "Design and optimisation of a novel asymmetric rotor structure for a PM-assisted synchronous reluctance machine," *IET Electric Power Applications*, Vol. 13, No. 5, 573–580, 2019.

[8] Liu, G., X. Du, G. Xu, and X. Fan, "Optimal design of an inset PM motor with assisted barriers and magnet shifting for improvement of torque characteristics," in *2017 IEEE International Magnetics Conference (INTERMAG)*, 1–1, Dublin, Ireland, 2017.

[9] Xu, M., G. Liu, Q. Chen, J. Ji, and W. Zhao, "Design and optimization of a fault tolerant modular permanent magnet assisted synchronous reluctance motor with torque ripple minimization," *IEEE Transactions on Industrial Electronics*, Vol. 68, No. 9, 8519–8530, 2021.

[10] Li, Z.-C., J.-P. Lu, W.-J. Wan, Y.-H. Lan, Y. Wang, D. Shi, W. Hong, and J.-X. Shen, "Torque ripple reduction with harmonics superposition and optimization for axially-segmented pm-assisted synchronous reluctance machines," *IEEE Transactions on Industry Applications*, Vol. 61, No. 5, 6973–6983, 2025.

[11] Qiao, Z., L. Shi, F. Li, H. Xu, T. Zhou, and W. Wang, "Characteristics analysis of magnetic-pole-shift in an asymmetric hybrid pole-permanent magnet-assisted synchronous reluctance motor," *IEEE Journal of Emerging and Selected Topics in Power Elec-*

tronics, Vol. 13, No. 2, 1394–1405, 2025.

[12] Zhao, W., C. Diao, D. Chen, Y. Liu, and X. Wang, "A permanent magnet concentrated-flux synchronous reluctance motor with torque improvement for unmanned ship propulsion," *IEEE Transactions on Transportation Electrification*, Vol. 11, No. 5, 10 822–10 835, 2025.

[13] Bonthu, S. S. R., M. T. B. Tarek, and S. Choi, "Optimal torque ripple reduction technique for outer rotor permanent magnet synchronous reluctance motors," *IEEE Transactions on Energy Conversion*, Vol. 33, No. 3, 1184–1192, 2018.

[14] Istenes, G., Z. Pusztai, P. Kőrös, Z. Horváth, and F. Friedler, "Kriging-assisted multi-objective optimization framework for electric motors using predetermined driving strategy," *Energies*, Vol. 16, No. 12, 4713, 2023.

[15] Sun, C., Q. Li, T. Fan, X. Wen, and Y. Li, "Multi-objective optimization design of external rotor permanent magnet machine for in-wheel applications," in *2023 24th International Conference on the Computation of Electromagnetic Fields (COMPUMAG)*, 1–4, Kyoto, Japan, 2023.

[16] Gözüaçık, E. and M. Akar, "Multi-physics and multi-objective design of an axial flux permanent magnet-assisted synchronous reluctance motor for use in electric vehicles," *Machines*, Vol. 13, No. 7, 555, 2025.

[17] Hua, Y., H. Zhu, and Y. Xu, "Multi-objective optimization design of bearingless permanent magnet synchronous generator," *IEEE Transactions on Applied Superconductivity*, Vol. 30, No. 4, 1–5, 2020.

[18] Hua, Y., H. Zhu, M. Gao, and Z. Ji, "Multiobjective optimization design of permanent magnet assisted bearingless synchronous reluctance motor using NSGA-II," *IEEE Transactions on Industrial Electronics*, Vol. 68, No. 11, 10 477–10 487, 2021.

[19] Zhang, H., G. Wang, J. Zhang, Y. Gao, W. Hua, and Y. Wang, "An improved kriging surrogate model method with high robustness for electrical machine optimization," *IEEE Transactions on Industry Applications*, Vol. 60, No. 5, 6799–6810, 2024.

[20] Ma, H., Y. Zhang, S. Sun, T. Liu, and Y. Shan, "A comprehensive survey on NSGA-II for multi-objective optimization and applications," *Artificial Intelligence Review*, Vol. 56, No. 12, 15 217–15 270, 2023.

[21] Chu, W. Q. and Z. Q. Zhu, "Average torque separation in permanent magnet synchronous machines using frozen permeability," *IEEE Transactions on Magnetics*, Vol. 49, No. 3, 1202–1210, 2012.